
CMS Physics Analysis Summary

Contact: cms-pog-conveners-jetmet@cern.ch

2010/03/10

Jets in 0.9 and 2.36 TeV pp Collisions

The CMS Collaboration

Abstract

During the LHC early commissioning phase, CMS recorded about 350k and 20k minimum bias events from proton-proton collisions at $\sqrt{s} = 900$ GeV and $\sqrt{s} = 2360$ GeV respectively. Three types of jets are reconstructed: jets from calorimeter energy depositions, from combined calorimeter and tracker information, and from particle flow candidates. We study the properties of inclusive jets and dijet events. The collision data are in good agreement with predictions from PYTHIA minimum bias events passed through the full CMS detector simulation.

1 Introduction

In 2009 CMS recorded roughly 350k and 20k minimum bias events from LHC proton-proton collisions at $\sqrt{s} = 900$ GeV and $\sqrt{s} = 2360$ GeV respectively. Here we present studies of jets, reconstructed from different detector inputs, with the intention to demonstrate that the jet reconstruction in CMS is performing well at these energies. First we examine a sample of **dijet events for which both jets with the highest transverse momentum p_T in the event are back-to-back in azimuth ϕ** . The topological selection of the dijet sample and the kinematic requirement that both jets should have sufficiently high p_T , suppress the contamination from fake jets arising from detector noise and beam losses. The resulting high purity dijet sample allows the study of jet properties with loose additional jet quality criteria and serves as a benchmark sample for the jet commissioning. Beyond the dijet selection, **we also report on the characteristics of jets inclusively**. The study of the inclusive jet sample is an essential jet commissioning step, as it examines the jet properties independently of the event topology and is relevant for every physics analysis with jets in the final state. In the absence of topological constraints, the purity of the inclusive jet sample is enhanced by applying tight kinematic selection requirements and jet quality criteria. This is considered necessary, as the inclusive jet sample is more sensitive to the instrumental backgrounds from the various CMS sub-systems than the dijet sample.

The results concerning both dijet and inclusive jet samples presented here, focus mostly on the data from the LHC proton-proton collisions at $\sqrt{s} = 900$ GeV because they provide about an order of magnitude more events compared to the sample recorded at $\sqrt{s} = 2360$ GeV.

Section 2 describes the different types of jet reconstruction employed by CMS which are studied here, and Section 3 refers to the jet energy calibration. Section 4 summarizes the jet quality criteria applied for each type of jet and motivates the different treatment of the dijet and inclusive jet samples. The selection of good quality minimum bias collision events is described in Section 5. The results of the dijet and inclusive jet analyses are presented in Sections 6 and 7 respectively. Section 8 summarizes the results.

2 Jet Reconstruction at CMS

Three different types of jet reconstruction are employed by CMS [1], characterized by the way that the sub-detector inputs are used during the jet finding procedure: calorimeter jets (Calo-Jets), jet-plus-tracks jets (JPTJets) and particle flow jets (PFJets).

Calorimeter jets are reconstructed using energy deposits in the electromagnetic and hadronic calorimeter cells, combined into *calorimeter towers* as inputs. **A calorimeter tower consists of one or more hadron calorimeter (HCAL) cells and the geometrically corresponding electromagnetic calorimeter (ECAL) crystals**. In the barrel region of the calorimeters ($|\eta| < 1.4$), the unweighted sum of one single HCAL cell and 5x5 ECAL crystals form a projective calorimeter tower. The association between HCAL cells and ECAL crystals is more complex in the endcap regions of the electromagnetic calorimeter ($1.4 < |\eta| < 3.0$). Beyond the coverage of the ECAL ($|\eta| > 3.0$), each calorimeter tower corresponds to one HCAL cell.

The **Jet-Plus-Tracks** (JPT) algorithm [2] corrects the energy and the direction of a calorimeter jet. It exploits the excellent performance of the CMS tracking detectors [3] to improve the p_T response and resolution of calorimeter jets (tracking coverage extends up to $|\eta| \approx 2.4$). **Charged particle tracks are associated with each calorimeter jet based on spatial separation in η - ϕ between the jet axis and the track momentum measured at the interaction vertex**. The associated tracks are classified as *in-cone tracks* if their projection onto the surface of the calorimeter (ECAL)

falls within the jet cone. Conversely, if they are bent outside the cone by the magnetic field, then they are called *out-of-cone tracks*. The momenta of both in-cone and out-of-cone tracks are then added to the energy of the associated calorimeter jet. For in-cone tracks the expected average energy deposition in the calorimeters is subtracted, based on the momentum of the track and the hypothesis that it originates from a charged pion.

The **Particle Flow** (PF) algorithm [4] aims to reconstruct, identify and calibrate each individual particle in the event by combining the information from all CMS sub-detector systems. PF particles are reconstructed as a combination of charged particle tracks and clusters in the electromagnetic and hadronic calorimeters, as well as signals in either of the two CMS pre-shower detectors and the muon system. Depending on which of the detector systems contribute to a single particle, it is identified as either an electron (track+ECAL), muon (track+ECAL+HCAL+Muon System), photon (ECAL), charged hadron (track+ECAL+HCAL), or neutral hadron (HCAL). The algorithm employs strategies to handle ambiguities stemming from overlapping detector signals to avoid information double-counting. Based on the particle type, the energy of each particle is calibrated. Charged hadrons are treated under the assumption that they are pions. As a result of the PF reconstruction, the inputs to the jet clustering are almost fully calibrated and the resulting higher level objects (jets) require small *a posteriori* energy corrections. A detailed description of the particle flow algorithm commissioning with $\sqrt{s} = 900$ GeV and $\sqrt{s} = 2360$ GeV collision data can be found in reference [5].

In addition to the jet properties, we also discuss the event variable $E_T^{\text{miss}}/\Sigma E_T$ where E_T^{miss} is the missing transverse energy and ΣE_T is the total transverse energy of the event. The $E_T^{\text{miss}}/\Sigma E_T$ variable is used here as a measure of the purity of the dijet and inclusive jet samples. The three corresponding algorithms to reconstruct E_T^{miss} at CMS, CaloMET, tcMET [6] and PFMET are described in [7] along with the respective analysis results from the $\sqrt{s} = 900$ GeV and $\sqrt{s} = 2360$ GeV collision events.

CMS plans to employ several jet clustering algorithms, e.g. anti- k_T [8], k_T [9, 10] and SIS-CONE [11], with different choices for the jet size parameter R . Jets in the studies presented here are reconstructed with the anti- k_T algorithm, $R = 0.5$, provided by an interface of the CMS software to the FASTJET package [12].

The lego and $\rho - \varphi$ views of a dijet event recorded by CMS in one of the $\sqrt{s} = 900$ GeV collision runs are shown in Figure 1. The red and blue boxes correspond to ECAL and HCAL energy deposits respectively, while the green lines represent charged particle tracks.

3 Jet Energy Corrections

Jet energy corrections need to be applied to account for the non-linear and non-uniform response of the CMS calorimeters. They associate, on average, the p_T of a reconstructed jet to the p_T of the corresponding particle jet. The latter is obtained by clustering with the same jet algorithm the stable particles produced during the hadronization process that follows the hard interaction.

The jet energy corrections used here, are derived from PYTHIA [13] QCD events from proton-proton collisions at $\sqrt{s} = 900$ GeV and $\sqrt{s} = 2360$ GeV which were further processed with the full, GEANT4 [14] based, CMS detector simulation. They consist of two stages: the relative (Rel) correction that makes the jet response uniform in η , by calibrating, on average, to the response in the central region of the calorimeters ($|\eta| < 1.3$); the absolute (Abs) correction that removes the p_T dependence of the jet response. The combined correction factor $C(p_T, \eta)$

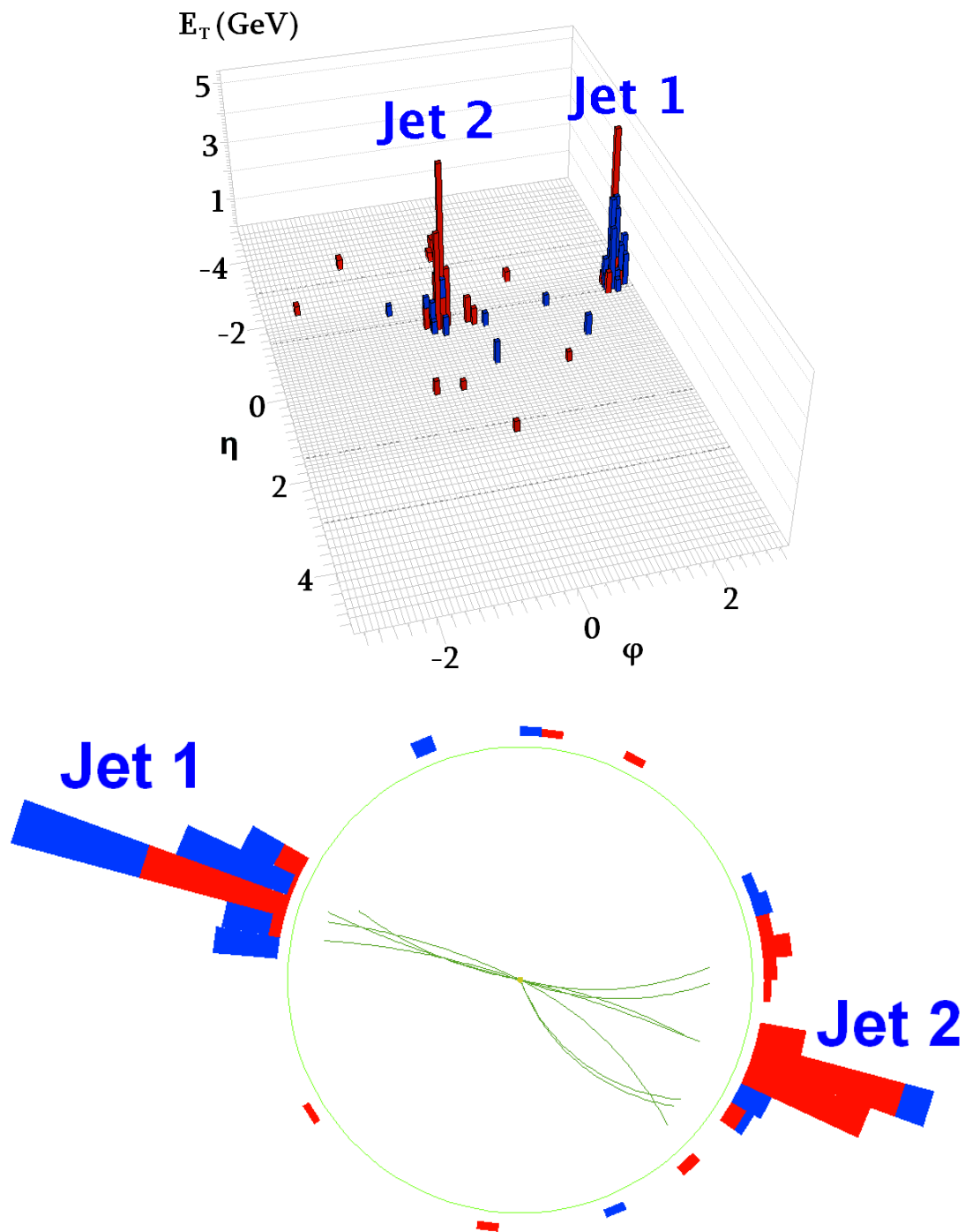


Figure 1: Lego (top) and $\rho - \phi$ (bottom) views of a dijet candidate event recorded during a $\sqrt{s} = 900 \text{ GeV}$ collision run by CMS. Charged particle tracks with $p_T > 1 \text{ GeV}$ are depicted as green lines. The transverse energies of ECAL and HCAL energy deposits contained in a single calorimeter tower and $E_T > 0.3 \text{ GeV}$ are represented by red and blue bars respectively. The transverse momenta of the two jets are measured to be 45 GeV and 37 GeV for calorimeter jets, 39 GeV and 33 GeV for JPT jets and 39 GeV and 31 GeV for particle flow jets.

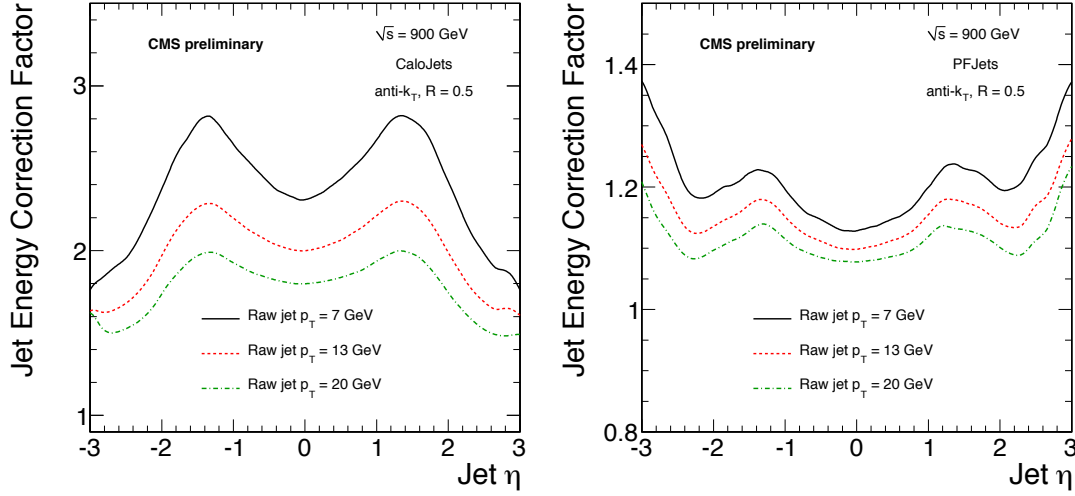


Figure 2: Jet energy correction factors derived from simulation for calorimeter jets (left) and particle flow jets (right) for $\sqrt{s} = 900$ GeV as a function of jet η for three different values of raw jet p_T : 7, 13 and 20 GeV. Note that the scale on the y -axis for the two types of jets is different.

multiplies each component of the jet momentum four-vector P_μ (components indexed by μ in the following):

$$P_\mu^{cor} = C(p_T, \eta) \times P_\mu \quad (1)$$

$$C(p_T, \eta) = \text{Rel}(\eta, p_T) \times \text{Abs}(p_T \times \text{Rel}(\eta, p_T)) \quad (2)$$

The MC jet energy corrections described above are applied to calorimeter jets and particle flow jets in data and simulation. Figure 2 shows the combined correction factors for calorimeter jets (left) and particle flow jets (right) at $\sqrt{s} = 900$ GeV. At low p_T , calorimeter jets need to be corrected by a large factor (up to ~ 3), while particle flow jets require a much smaller correction (up to ~ 1.4). The corresponding correction factors for $\sqrt{s} = 2360$ GeV show similar characteristics.

The JPT algorithm is designed to restore the energy scale of calorimeter jets which is due to the charged hadrons. The energies of JPT jets are not further corrected for the calorimeter response of neutral hadron constituents, which accounts for a less than 10% residual correction and is comparable to the the calibration applied to the particle flow jets in the central region.

4 Jet Quality Criteria

CMS has developed jet quality criteria (“**Jet ID**”) for calorimeter jets [15] and particle flow jets which are found to retain the vast majority of real jets in the simulation while rejecting most fake jets in pure noise non-collision data samples (e.g. from cosmic triggers or triggers on empty bunches during LHC operation). For both types of jets two sets of criteria are defined: loose and tight. The loose cuts are applied to the two leading jets in the dijet analysis, for which the topological selection is expected to suppress most of the fake jets due to instrumental effects. The tight criteria are necessary to select an inclusive jet sample which is sufficiently pure in the absence of any topological selection. JPT jets are treated as calorimeter jets with respect to these quality criteria. The loose and tight JetID criteria for calorimeter jets and JPT jets are summarized in Table 1 and for particle flow jets in Table 2.

variable	$ \eta $	loose	tight
EMF	< 2.6	> 0.01	> 0.01
n_{hits}^{90}	-	> 1	> 4
f_{HPD}	-	< 0.98	< 0.98
f_{RBX}	-	-	< 0.98
σ_{η}	-	-	> 0.01
σ_{φ}	-	-	> 0.01

Table 1: Loose (dijet analysis) and tight (inclusive jet analysis) calorimeter jet quality criteria. EMF = electromagnetic energy fraction; σ_{η} and σ_{φ} refer to the E_T -weighted jet width in η and φ respectively; for detailed explanations of n_{hits}^{90} , f_{HPD} and f_{RBX} refer to Ref. [15].

variable	$ \eta $	loose	tight
CHF	< 2.4	> 0.0	> 0.0
NHF	-	< 1.0	< 0.9
CEF	-	< 1.0	< 1.0
NEF	-	< 1.0	< 0.9

Table 2: Loose (dijet analysis) and tight (inclusive jet analysis) particle flow jet quality criteria. CHF = charged hadron fraction; NHF = neutral hadron fraction; CEF = charged electromagnetic (electron) fraction; and NEF = neutral electromagnetic (photon) fraction.

5 Samples and Event Selection

For both the dijet and inclusive jet analysis, only those 15 (1) collision runs at $\sqrt{s} = 900$ GeV ($\sqrt{s} = 2360$ GeV) are considered where the calorimeters and tracking detectors were fully operational. To select minimum bias events, Level-1 triggers were used which selected the correct LHC bunch crossing as well as required activity in the beam scintillation detectors on each side of the CMS detector. A veto on Level-1 triggers which indicate the occurrence of beam halo effects was also applied. The events were further filtered based on their signature in the pixel detector: the fraction of high-purity tracks [3] with respect to the total number of tracks was required to be at least 20% for events with at least ten tracks. Furthermore, the reconstruction of one good primary vertex (PV) is required with $|z(\text{PV})| < 15$ cm and $n_{\text{dof}}(\text{PV}) \geq 5.0$, which means that at least four tracks are considered in the vertex fit. $z(\text{PV})$ represents the position of the proton-proton collision along the beam-line and $z = 0$ indicates the center of the CMS detector. The numbers of events after each selection requirement are summarized in Table 3 for both the $\sqrt{s} = 900$ GeV and $\sqrt{s} = 2360$ GeV collision samples.

6 Dijet Analysis

Dijet events are selected by requiring the two highest transverse momentum jets (“leading jets”) to be back-to-back in azimuth φ , $||\Delta\varphi(j_1, j_2) - \pi| < 1.0$. Both jets are required to be within

Selection	$\sqrt{s} = 900$ GeV	$\sqrt{s} = 2360$ GeV
Data Quality and Trigger	214133	11832
Primary Vertex	164703	9685

Table 3: Number of events after each selection requirement for the $\sqrt{s} = 900$ GeV and $\sqrt{s} = 2360$ GeV collision samples.

	CaloJets	JPTJets	PFJets
p_T^{\min}	10 GeV	8 GeV	8 GeV
η^{\max}	3.0	2.0	3.0

Table 4: Minimum transverse momenta p_T^{\min} and maximum pseudorapidities η^{\max} for calorimeter jets, JPT jets and particle flow jets in the dijet analysis.

Selection	$\sqrt{s} = 900 \text{ GeV}$			$\sqrt{s} = 2360 \text{ GeV}$		
	CaloJets	JPTJets	PFJets	CaloJets	JPTJets	PFJets
$p_T > p_T^{\min}, \eta < \eta^{\max}$	574	418	719	98	90	172
$ \Delta\varphi(j_1, j_2) - \pi < 1.0$	339	268	556	55	58	111
loose JetID	246	218	531	46	48	111

Table 5: Number of events after each dijet selection requirement for calorimeter jets, JPT jets and particle flow jets at $\sqrt{s} = 900 \text{ GeV}$ and $\sqrt{s} = 2360 \text{ GeV}$.

$|\eta| < 3.0$, with the exception of JPT jets ($|\eta| < 2.0$), corresponding to the range for which the JPT algorithm is currently defined. Furthermore, the two leading jets are required to have $p_T > 10 \text{ GeV}$, $p_T > 8 \text{ GeV}$ and $p_T > 8 \text{ GeV}$ for calorimeter jets, JPT jets and particle flow jets, respectively (see Table 4). Finally, the loose jet quality criteria described in Section 4 are applied to the two leading jets, in order to reject events with fake jets due to detector noise that survived the dijet topological selection. The number of events after each selection requirement are summarized in Table 5 for calorimeter jets, JPT jets and particle flow jets at both $\sqrt{s} = 900 \text{ GeV}$ and $\sqrt{s} = 2360 \text{ GeV}$. The difference in the number of jets between the jet types is caused by the different kinematic selection, enhanced by the steeply falling p_T spectrum. Note that all jet distributions shown in this section contain only information about the two leading jets. The MC distributions are normalized to the number of selected data events after the application of all selection requirements.

The data to simulation comparisons of kinematic and topological calorimeter jet distributions are shown in Figure 3 for $\sqrt{s} = 900 \text{ GeV}$. Good agreement with the simulation is observed for all distributions: the $|\Delta\varphi(j_1, j_2)|$ distribution is well described and shows the expected dijet behaviour, peaked at π and steeply falling towards smaller values, indicating high sample purity. The latter is also demonstrated in the $E_T^{\text{miss}}/\Sigma E_T$ distributions: pure dijet events are expected to be well balanced with small E_T^{miss} compared to ΣE_T , caused by the finite jet resolution. The fact that the $E_T^{\text{miss}}/\Sigma E_T$ variable is concentrated at values much smaller than 0.5 is a clear indication that the dijet sample is enriched in true jets from the hard interaction. The dijet invariant mass m_{jj} shows good agreement between data and simulation. It should be noted that the ‘‘turn-on’’ shape of the dijet invariant mass is caused by the p_T requirement on both leading jets which restricts the kinematic phase-space.

The corresponding distributions for JPT and particle flow jets at $\sqrt{s} = 900 \text{ GeV}$ are shown in Figures 4 and 5. In both cases, the agreement between data and simulation is good as well. The JPT jet p_T and dijet mass spectra are more steeply falling than the corresponding calorimeter and particle flow jets, due to the different pseudorapidity range. Furthermore, the large fraction of calorimeter jets observed at high transverse momenta with respect to the particle flow jets is attributed to the more significant impact of the resolution smearing for calorimeter jets. This smearing is caused by the finite jet energy resolution combined with the steeply falling p_T spectrum which leads to jet migration to higher p_T bins. This effect appears in all types of jets, but is more pronounced for calorimeter jets whose resolution is substantially worse at low

transverse momenta.

Beyond the kinematic variables discussed above, the modelling of the interplay between the various subsystems involved in the reconstruction of each type of jet by the simulation is essential to their successful application in physics analysis. Figures 6, 7 and 8 provide further information about the composition of calorimeter jets, JPT jets and particle flow jets at $\sqrt{s} = 900$ GeV respectively: the number of input objects clustered into calorimeter and particle flow jets, the electromagnetic energy fraction EMF of calorimeter jets and JPT jets, the number of tracks considered by the JPT algorithm, and the charged hadron, neutral hadron and photon fractions for particle flow jets. Note that the EMF for JPT jets is computed from the original calorimeter jet alone and is not modified with tracking information. The composition plots for all three type of jets show good agreement with the simulation without statistically significant differences.

Finally, the p_T spectra of calorimeter jets, JPT jets and particle flow jets at $\sqrt{s} = 2360$ GeV are shown in Figure 9 which agree with the simulation prediction.

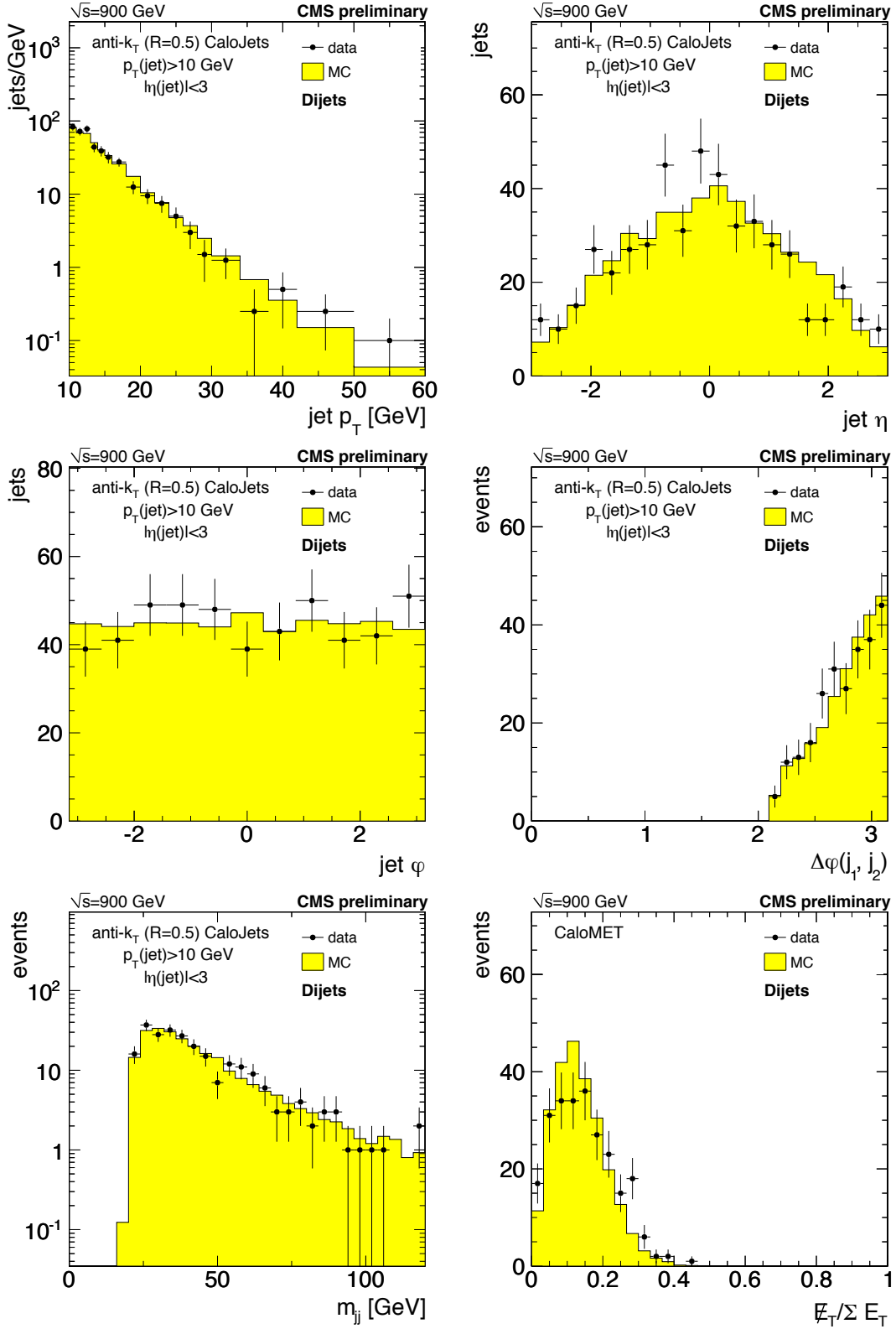


Figure 3: Comparisons of data and MC distributions for the two leading calorimeter jets for selected $\sqrt{s} = 900$ GeV dijet events: jet p_T (top left), jet η (top right), jet ϕ (center left), $|\Delta\phi(j_1, j_2)|$ (center right) and the invariant dijet mass m_{jj} (bottom left). The transverse missing energy E_T^{miss} divided by the ΣE_T , both calculated from calorimeter towers ("CaloMET") is also shown (bottom right). Jets are reconstructed with the anti- k_T $R = 0.5$ algorithm.

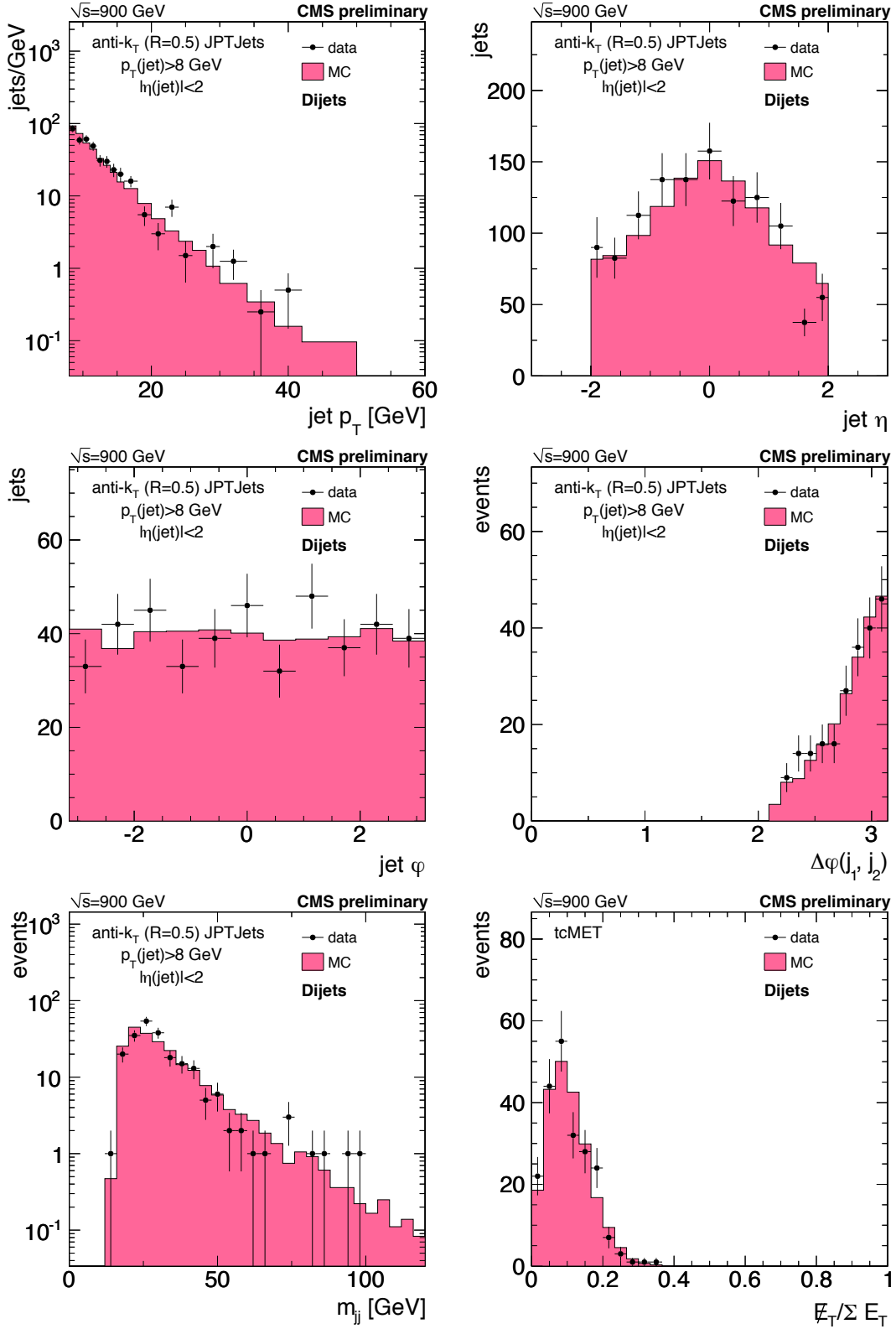


Figure 4: Comparisons of data and MC distributions for the two leading jet-plus-track (JPT) jets for selected $\sqrt{s} = 900$ GeV dijet events: jet p_T (top left), jet η (top right), jet ϕ (center left), $|\Delta\phi(j_1, j_2)|$ (center right) and the invariant dijet mass m_{jj} (bottom left). The transverse missing energy E_T^{miss} divided by the ΣE_T , both calculated from calorimeter towers and tracks (“tcMET”) is also shown (bottom right). Jets are reconstructed with the anti- k_T $R = 0.5$ algorithm.

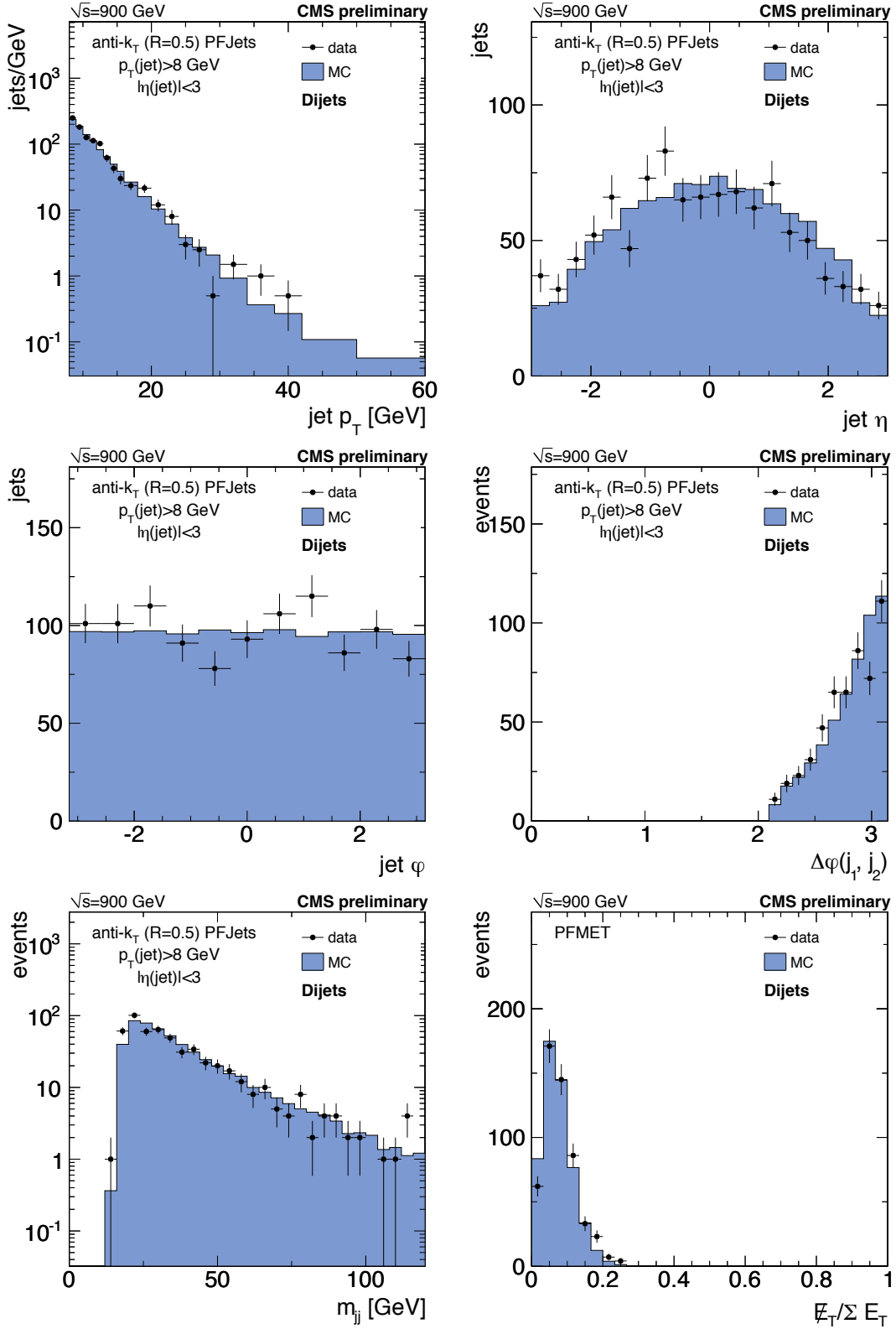


Figure 5: Comparisons of data and MC distributions for the two leading particle flow jets for the selected $\sqrt{s} = 900$ GeV dijet events: jet p_T (top left), jet η (top right), jet ϕ (center left), $|\Delta\phi(j_1, j_2)|$ (center right) and the invariant dijet mass m_{jj} (bottom left). The transverse missing energy E_T^{miss} divided by the ΣE_T , both calculated from particle flow particles (“PFMET”) is also shown (bottom right). Jets are reconstructed with the anti- k_T $R = 0.5$ algorithm.

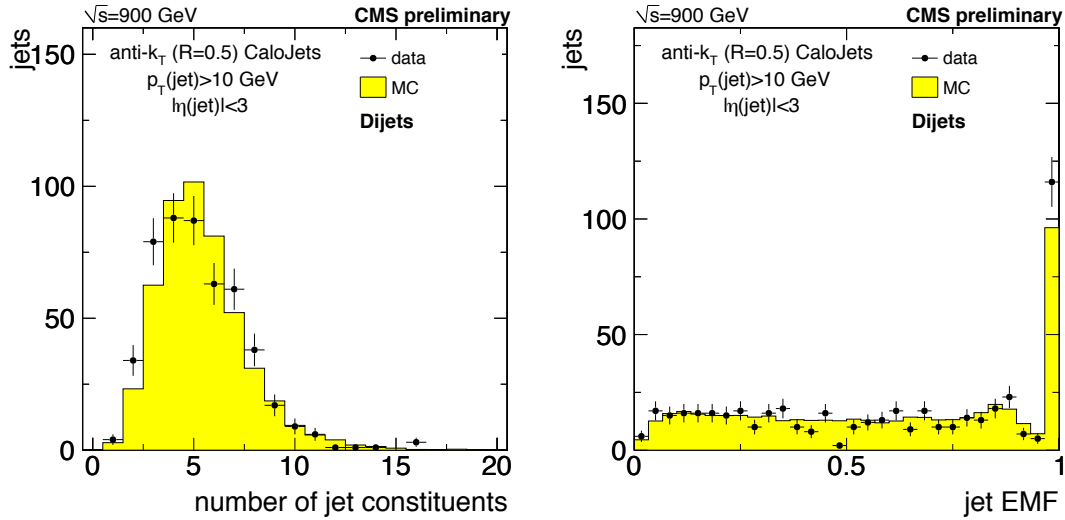


Figure 6: Comparisons of data and MC jet composition distributions for the two leading calorimeter jets for selected $\sqrt{s} = 900$ GeV dijet events: number of jet constituents (left) and the fraction of jet energy contributed by electromagnetic calorimeter deposits EMF (right).

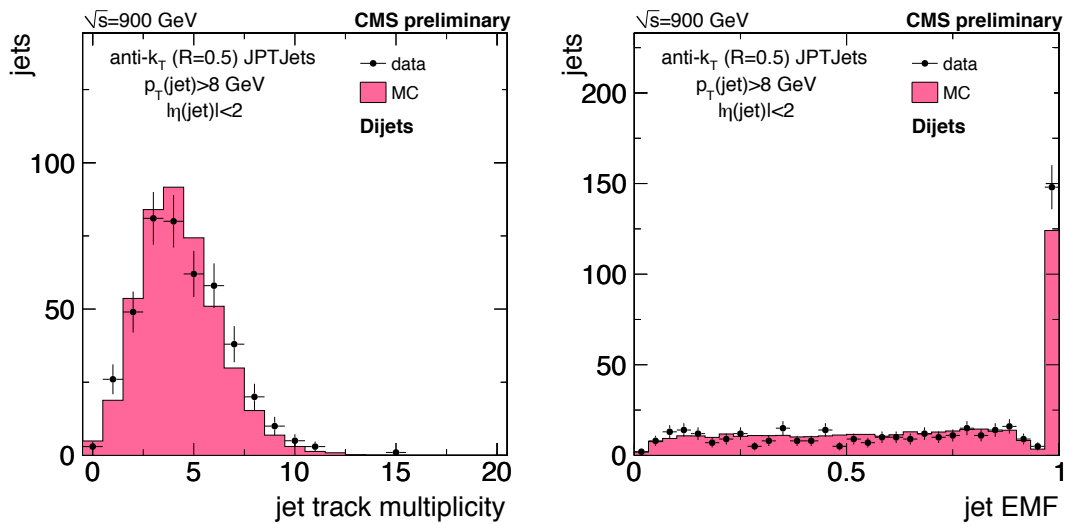


Figure 7: Comparisons of data and MC jet composition distributions for the two leading JPT jets for selected $\sqrt{s} = 900$ GeV dijet events: jet track multiplicity (left) and fraction of jet energy contributed by electromagnetic calorimeter deposits EMF (right).

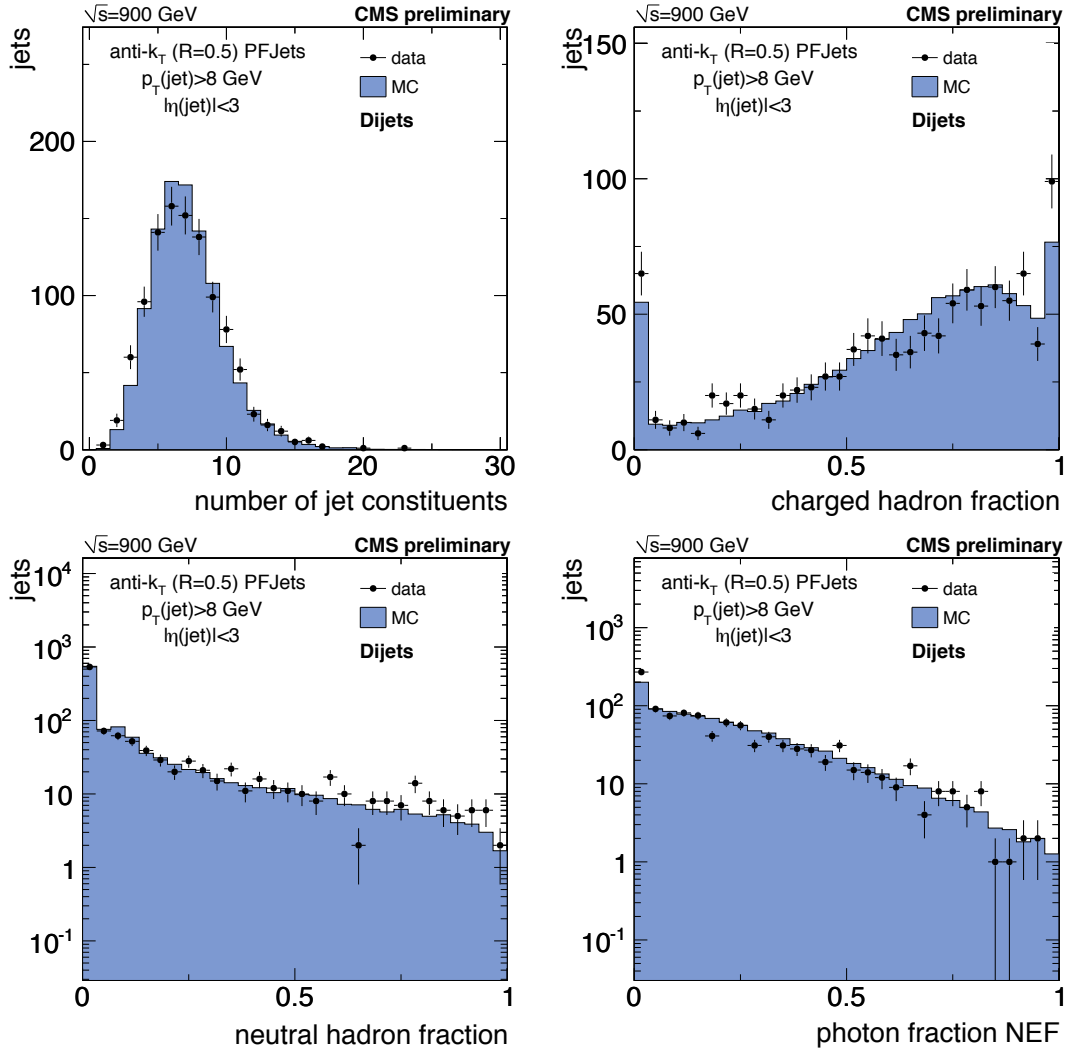


Figure 8: Comparisons of data and MC jet composition distributions for the two leading particle flow jets for selected $\sqrt{s} = 900$ GeV dijet events: total number of jet constituents (top left), the fraction of jet energy contributed by charged hadrons, CHF (top right), the fraction of jet energy carried by neutral hadrons, NHF (bottom left) and the neutral electromagnetic (photon) fraction, NEF (bottom right).

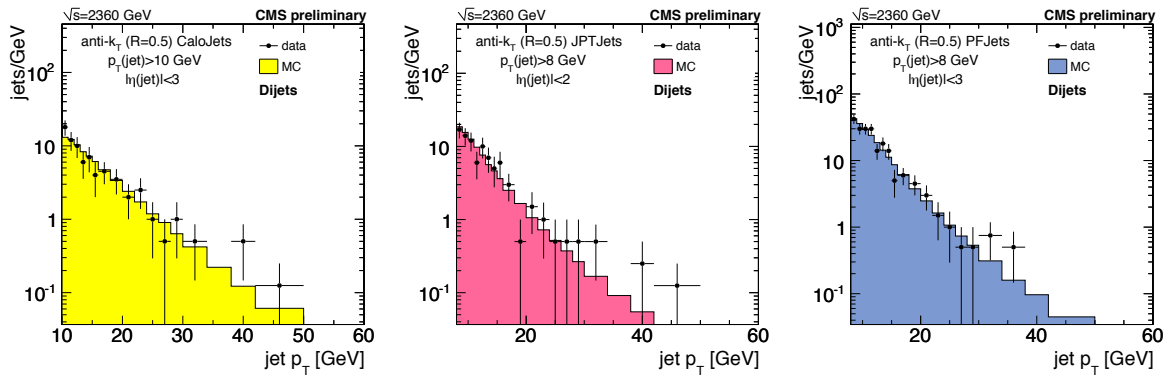


Figure 9: Comparisons of data and MC jet p_T spectra distributions for the two leading calorimeter jets (left), JPT jets (center) and particle flow jets (right) for selected $\sqrt{s} = 2360$ GeV dijet events.

	CaloJets	JPTJets	PFJets
p_T^{\min}	15 GeV	13 GeV	10 GeV
η^{\max}	2.6	2.0	3.0

Compare to:		
10 GeV	8 GeV	8 GeV
3.0	2.0	3.0

Table 6: Minimum transverse momenta p_T^{\min} and maximum pseudorapidities η^{\max} for calorimeter jets, JPT jets and particle flow jets in the inclusive jet analysis.

Selection	$\sqrt{s} = 900 \text{ GeV}$			$\sqrt{s} = 2360 \text{ GeV}$		
	CaloJets	JPTJets	PFJets	CaloJets	JPTJets	PFJets
$p_T > p_T^{\min}, \eta < \eta^{\max}$	1462	588	2499	199	107	496
tight JetID	459	302	2088	104	68	444

Table 7: Number of jets after each inclusive jet selection requirement for calorimeter jets, JPT jets and particle flow jets at $\sqrt{s} = 900 \text{ GeV}$ and $\sqrt{s} = 2360 \text{ GeV}$.

7 Inclusive Jet Analysis

As explained in Section 1, the inclusive jet study is essential for the overall understanding of jet performance in CMS and is more challenging to perform, due to the absence of a specific event topology that naturally suppresses instrumental backgrounds. The inclusive jet samples are composed of all jets in events satisfying the selection described in Section 5 with $|\eta| < \eta^{\max}$, $p_T > p_T^{\min}$, and satisfying the tight JetID cuts introduced in Section 4 aiming to select as pure a jet sample as possible. The p_T^{\min} and η^{\max} values for each type of jet are summarized in Table 6. The choice of different kinematic thresholds and pseudorapidity ranges for the three jet reconstruction types reflects their different properties: JPT and particle flow jets have better energy resolution at low p_T than the calorimeter jets and the latter require a much larger energy correction factor. The different pseudorapidity ranges are determined from the reconstruction applicability of the specific jet type (JPT is applied up to $|\eta| = 2$) and the corresponding JetID (the EMF selection criterion for calorimeter jets is very efficient up to $|\eta| = 2.6$). In addition, noise-only jet studies indicate that the p_T cuts employed here reject the largest fraction of fake jets. The number of jets after each selection requirement are listed in Table 7 for $\sqrt{s} = 900 \text{ GeV}$ and $\sqrt{s} = 2360 \text{ GeV}$. The difference in the number of jets between the jet types is caused by the different kinematic selection, enhanced by the steeply falling p_T spectrum.

The results for calorimeter jets, JPT jets and particle flow jets at $\sqrt{s} = 900 \text{ GeV}$ are shown in Figures 10, 11 and 12, respectively where the MC distributions are normalized to the number of selected jets in the data sample after the application of all selection requirements. The corresponding p_T distributions at $\sqrt{s} = 2360 \text{ GeV}$ for calorimeter jets, JPT jets and particle flow jets are shown in Figure 13. The agreement between data and simulation events is good for all considered distributions and the results confirm the observations of the dijet analysis regarding the good modelling of the collision data by the simulation. They furthermore indicate that the analysis of inclusive jets given the applied kinematic constraints and jet quality criteria is not significantly affected by the presence of fake jets due to instrumental backgrounds. This is supported by the $E_T^{\text{miss}}/\Sigma E_T$ distribution in Figure 10 for those events where at least one calorimeter jet satisfies the selection requirements. Fake jets tend to produce maximally unbalanced events, which would be seen in the $E_T^{\text{miss}}/\Sigma E_T$ distribution (shifted towards $E_T^{\text{miss}}/\Sigma E_T > 0.5$).

The inclusive jet p_T spectrum of calorimeter jets is found to extend to higher values than particle flow jets, as explained in Section 6. Also, the observed difference in the shapes of the η distributions of the three types of jets originate from the different p_T thresholds applied.

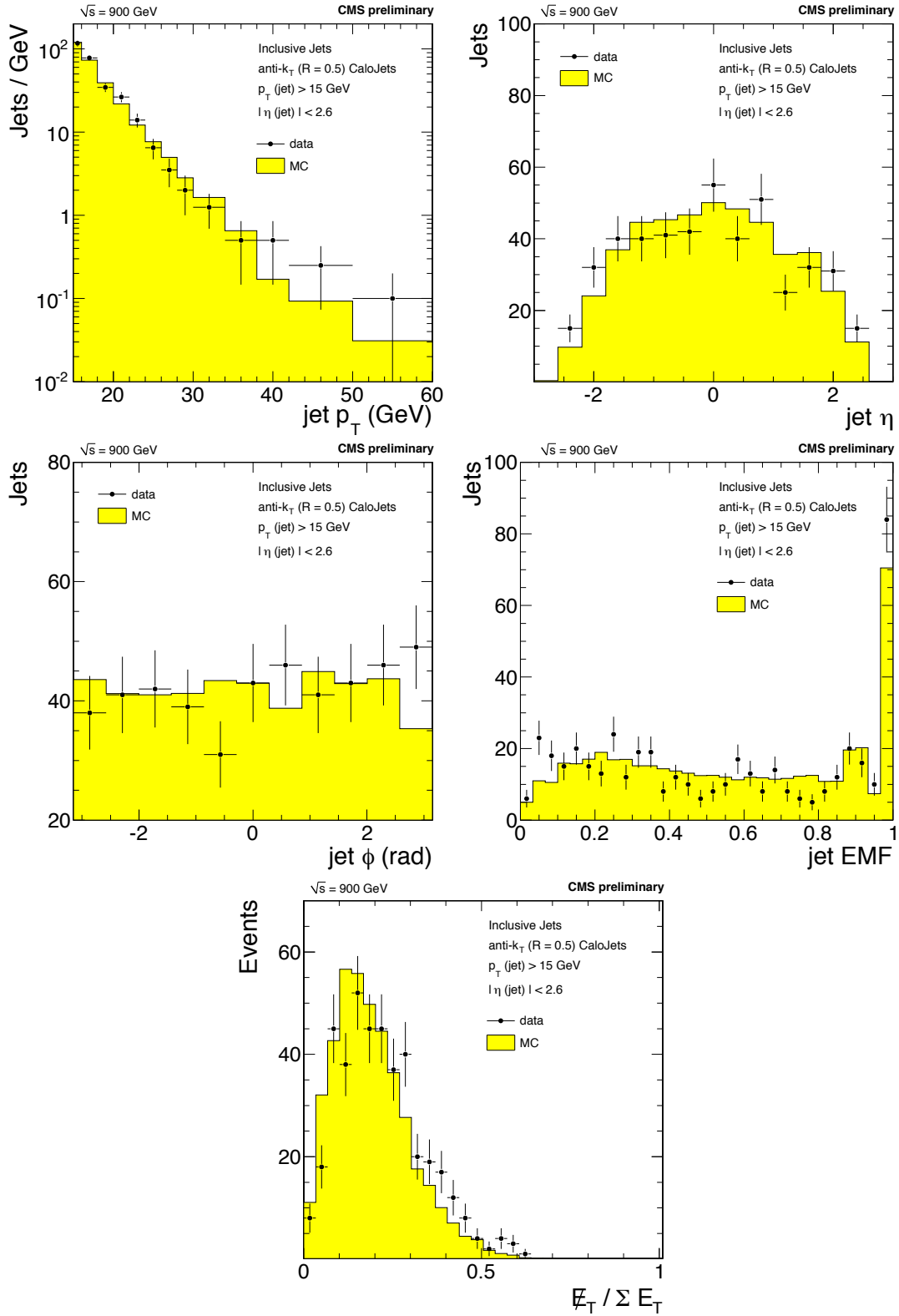


Figure 10: Comparisons of data and MC inclusive calorimeter jet distributions at $\sqrt{s} = 900$ GeV: jet p_T (top left), jet η (top right), jet ϕ (center left) and jet electromagnetic fraction EMF (center right). The $E_T^{\text{miss}} / \sum E_T$ distribution for events with at least one selected calorimeter jets is shown at the bottom.

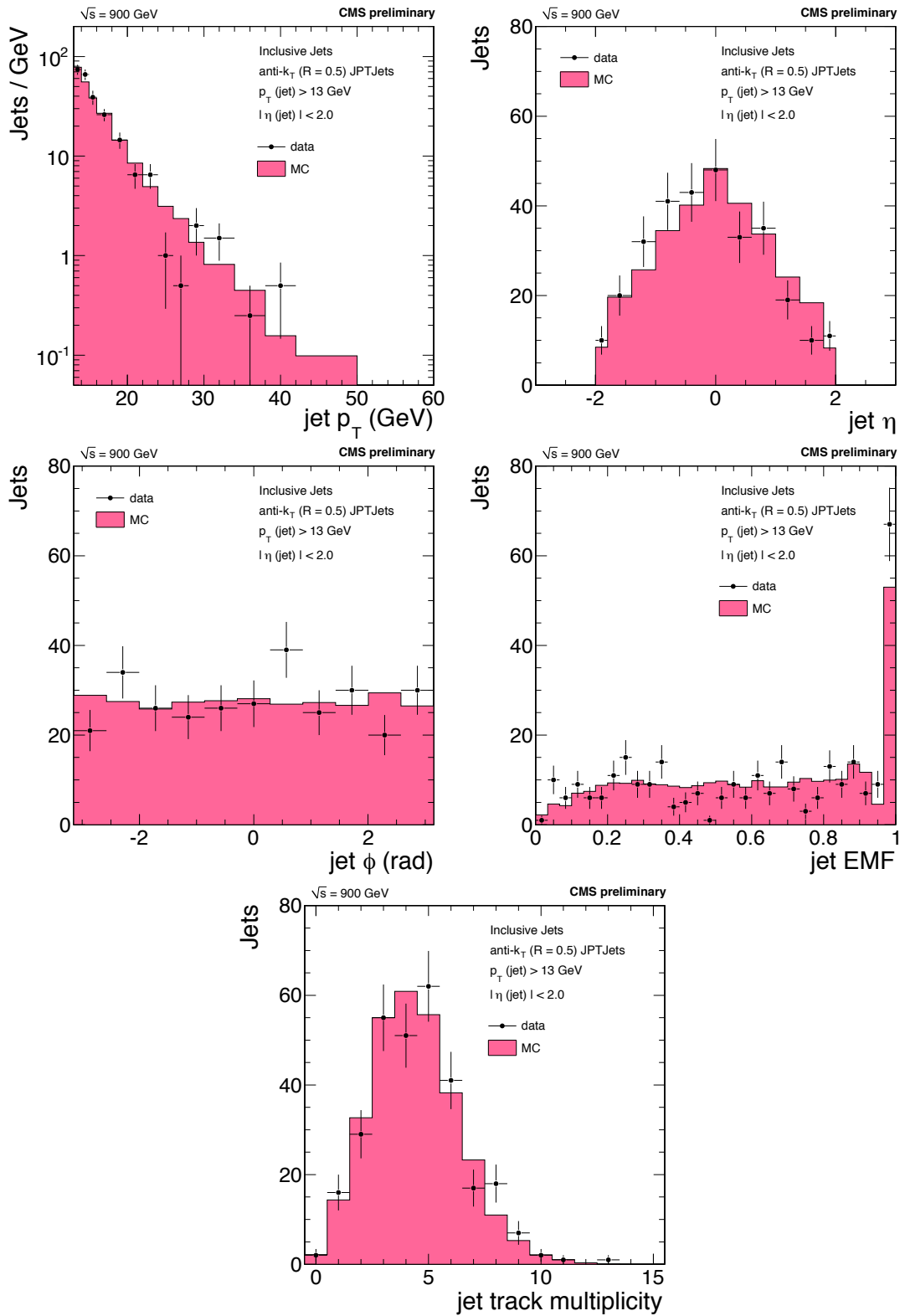


Figure 11: Comparisons of data and MC inclusive JPT jet distributions at $\sqrt{s} = 900$ GeV: jet p_T (top left), jet η (top right), jet ϕ (center left), jet electromagnetic fraction EMF (center right) and the number of tracks considered by the JPT algorithm to correct each jet N_{trk} (bottom).

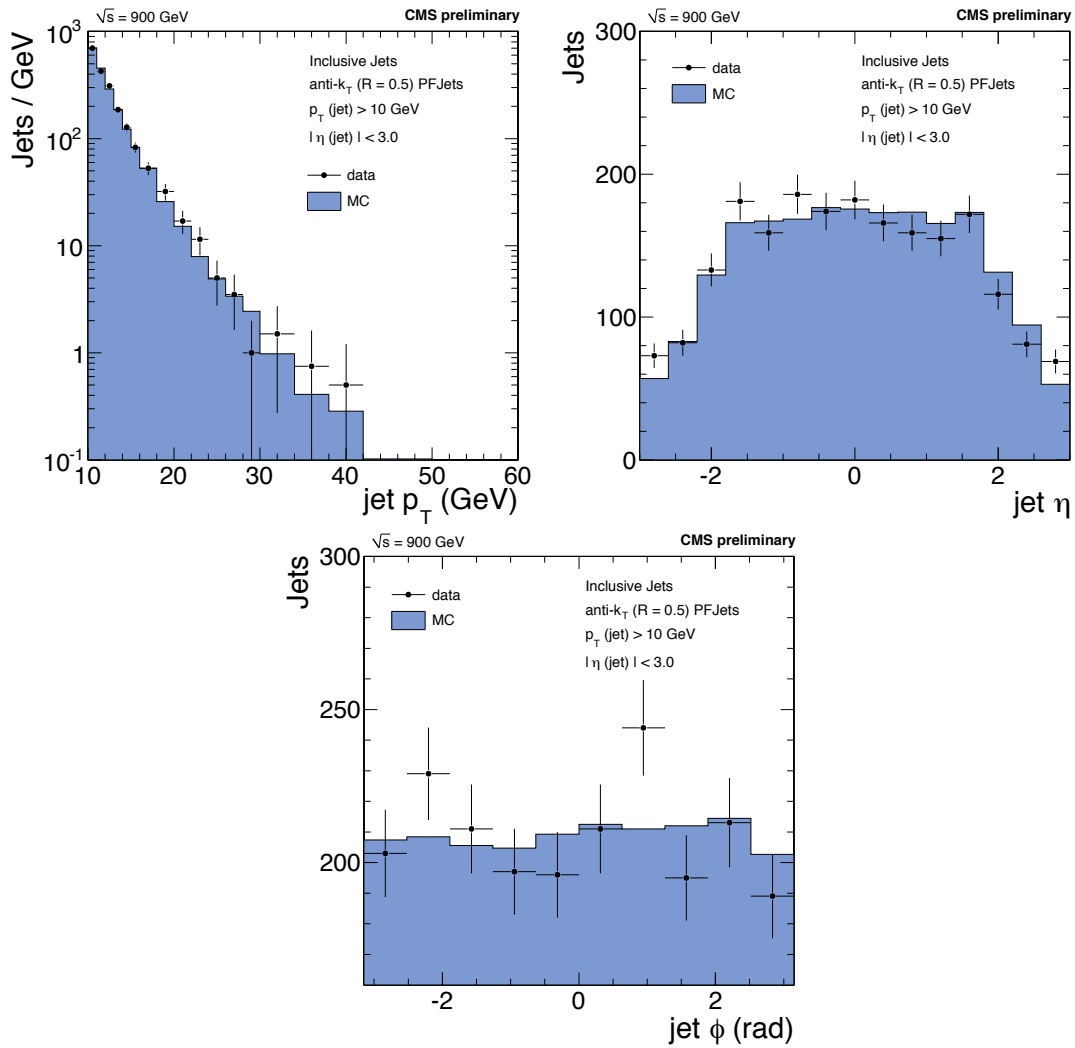


Figure 12: Comparisons of data and MC inclusive particle flow jet distributions at $\sqrt{s} = 900$ GeV: jet p_T (top left), jet η (top right) and jet ϕ (bottom).

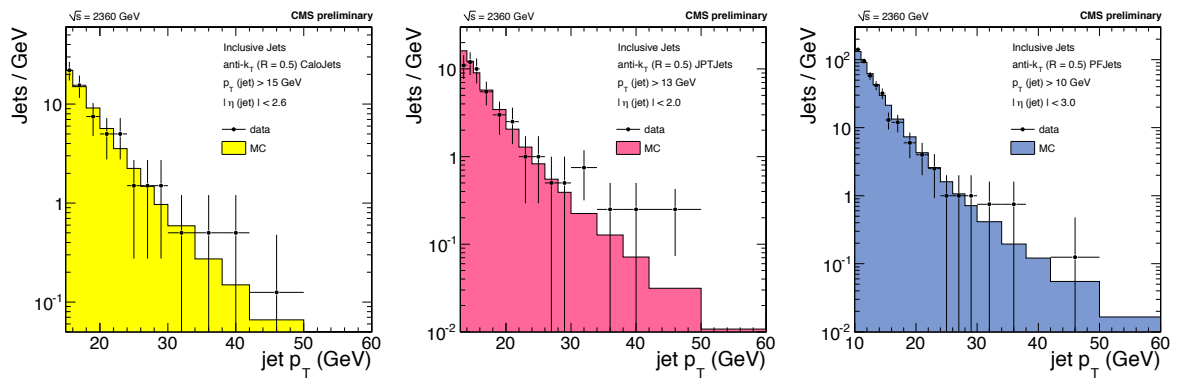


Figure 13: Comparisons of data and MC inclusive calorimeter (left), JPT (center) and particle flow jet p_T spectra.

8 Summary

We have presented studies of jet properties from proton-proton collisions at $\sqrt{s} = 900$ GeV and $\sqrt{s} = 2360$ GeV recorded by CMS during the early LHC commissioning phase in 2009.

Three different techniques to reconstruct jets in CMS have been considered: calorimeter jets, jet-plus-trackjets and particle flow jets. The properties of jets have been studied in two distinct samples: the dijet sample and the inclusive jet sample. The purity of the dijet sample is achieved by applying topological constraints and loose jet quality criteria, and of the inclusive sample by imposing tight jet quality criteria for each jet algorithm type. The comparison between data and simulation predictions for the dijet and inclusive jet samples and for all types of jets show good agreement. The simulation models well the kinematic distributions and the internal properties of jets measured in data despite the softness of the jet p_T selection.

References

- [1] CMS Collaboration, "The CMS Experiment at the CERN LHC", *JINST* **3** (2009) S08004.
- [2] CMS Collaboration, "Jet Plus Tracks Algorithm for Calorimeter Jet Energy Corrections in CMS", *CMS PAS JME-09-002* (2009).
- [3] CMS Collaboration, "Tracking and Vertexing Results from First Collisions", *CMS PAS TRK-10-001* (2010).
- [4] CMS Collaboration, "Particle-Flow Event Reconstruction in CMS and Performance for Jets, E_T^{miss} , and Taus", *CMS PAS PFT-09-001* (2009).
- [5] CMS Collaboration, "Particle flow reconstruction of 0.9 TeV and 2.36 TeV collision events in CMS", *CMS PAS PFT-10-001* (2010).
- [6] CMS Collaboration, "Performance of Track-Corrected Missing ET in CMS", *CMS PAS JME-09-010* (2009).
- [7] CMS Collaboration, "Performance of Missing Transverse Energy Reconstruction in $\sqrt{s} = 900$ GeV and 2360 GeV pp Collision Data", *CMS PAS JME-10-002* (2010).
- [8] M. Cacciari, G. P. Salam, and G. Soyez, "The anti-kt jet clustering algorithm", *JHEP* **0804:063** (2008).
- [9] S. Catani, Y. L. Dokshitzer, M. H. Seymour et al., "Longitudinally invariant Kt clustering algorithms for hadron hadron collisions", *Nucl.Phys.B* **406** (1993) 187–224.
- [10] S. D. Ellis and D. E. Soper, "Successive Combination Jet Algorithm For Hadron Collisions", *Phys.Rev.D* **48** (1993) 3160.
- [11] G. P. Salam and G. Soyez, "A practical seedless infrared-safe cone jet algorithm", *JHEP* **0507:086** (2007).
- [12] M. Cacciari and G. P. Salam, "Dispelling the N^3 myth for the Kt jet-finder", *Phys.Lett.B* **641** (2006) 57–61.
- [13] T. Sjostrand, S. Mrenna, and P. Skands, "PYTHIA 6.4 physics and manual", *JHEP* **05:026** (2007).

- [14] S. Agostinelli and et al., “Geant 4 – A Simulation Toolkit”, *Nucl.Inst.A* **506** (2003) 250–303.
doi:10.1016/S0168-9002(03)01368-8.
- [15] **CMS** Collaboration, “Calorimeter Jet Quality Criteria for the First CMS Collision Data”,
CMS PAS JME-09-008 (2009).